ELSEVIER

Contents lists available at ScienceDirect

Applied Catalysis A, General

journal homepage: www.elsevier.com/locate/apcata





Heterogeneous photo-Fenton-like degradation of emerging pharmaceutical contaminants in wastewater using Cu-doped MgO nanoparticles

Manoj Silva a,1 , John P. Baltrus b,2 , Clinton Williams c,3 , Allan Knopf c , Lihua Zhang d , Jonas Baltrusaitis a,4,*

- a Department of Chemical and Biomolecular Engineering, Lehigh University, B336 Iacocca Hall, 111 Research Drive, Bethlehem, PA 18015, USA
- ^b National Energy Technology Laboratory, US Department of Energy, 626 Cochrans Mill Road, Pittsburgh, PA 15236, USA
- ^c USDA-ARS, US Arid Land Agricultural Research Center, 21881N. Cardon Ln, Maricopa, AZ, 85138, USA
- ^d Brookhaven National Laboratory, Center for Functional Nanomaterials, Upton, NY 11973, USA

ARTICLEINFO

Keywords:

Heterogeneous photo-Fenton Catalysis Nanoparticles Wastewater treatment Emerging contaminants

ABSTRACT

A facile thermal decomposition method was utilized to synthesize mesoporous Cu-doped MgO nanoparticles. These Cu-MgO nanoparticles were shown to be efficient photo-Fenton-like catalysts for degrading emerging pharmaceutical contaminants in wastewater and completely oxidized salicylic acid within 1 h under optimized conditions. Tetracycline was shown to be converted to other intermediates with a large portion of it undergoing full mineralization. Batch experiments were conducted to demonstrate the effects of Cu loading on MgO, overall catalyst loading, and H_2O_2 concentration on the salicylic acid and tetracycline conversion and rate constants. Quenching experiments revealed that both *OH radicals or $HO_2^{\bullet}/^{\bullet}O_2^{-}$ radicals were involved in the reaction, with the latter showing a higher contribution. The surface dissolution of MgO was shown to increase solution pH which completely prevented Cu from leaching out while retaining high activity. The catalyst reusability was shown to be satisfactory with high activity and conversion being preserved over five cycles.

1. Introduction

Water is an essential component of the ecosystem and its security has become a key issue facing society. Access to clean water has been a significant challenge in the past few decades and will continue to be an issue in the foreseeable future provided that four billion people face water scarcity for at least one month every year [1,2]. Presently, the water sector is amid the Fourth Revolution, which involves closing the loop in water use and establishing water conservation and reuse strategies [3]. A rising threat to water purification and reuse in recent years has been pharmaceuticals which act as emerging contaminants due to the increasing population and urbanization leading to greater rates of their discharge. These compounds are ubiquitous in wastewater due to the use of personal care products and medicines at the residential level, as well as due to the pharmaceutical industry and hospital waste [4]. Due to their long lifetimes in water and their adverse effects on human

health and ecosystems, remediation of these contaminants is of utmost importance in working toward safe water reuse [4–6].

Advanced oxidation processes (AOPs) have previously been utilized as a method of removing emerging contaminants from wastewater [7,8]. AOPs utilize radical species generated in situ as oxidants to degrade various organic species present in water. In particular, the Fenton reaction, which utilizes the ${\rm Fe}^{2+}/{\rm Fe}^{3+}$ redox cycle, as well as other metal centers, such as Cu, Mn, Ru, Cr, and Co, has been reported in the literature to produce reactive radicals from ${\rm H_2O_2}$ [9–13]. Cu is the second most studied metal for Fenton-like reactions and given its non-toxic nature and faster kinetics of reactive oxygen species (ROS) production compared to Fe, it is desirable as a catalyst for this reaction [9,14–16]. Cu^+ reacts with ${\rm H_2O_2}$ rapidly to form radical species and Cu²⁺ while Cu²⁺ can be photo reduced back to Cu⁺ using a light source [13,17] via Eqs. (1) and (2).

E-mail address: job314@lehigh.edu (J. Baltrusaitis).

- ¹ 0000-0002-5353-006X.
- 2 0000-0003-3253-9193.
- ³ 0000-0002-2554-5061.
- ⁴ 0000-0001-5634-955X.

 $^{^{\}ast}$ Corresponding author.

$$Cu^{+} + H_{2}O_{2} \rightarrow Cu^{2+} + HO^{\bullet} + OH^{-}k = 1 \times 104M - 1 * s^{-1}$$
 (1)

$$Cu^{2+} + H_2O_2 \rightarrow Cu^+ + HO_2^{\bullet} + H^+k = 460M - 1 * s^{-1}$$
 (2)

Since the step in (2) of the Fenton-like redox cycling of Cu^{2+}/Cu^+ is accelerated by light, photocatalytic treatment methods to remove emerging pharmaceutical contaminants become viable methods to ensure safe water reuse.

Controlling parameters such as catalyst loading, pH, and H₂O₂ concentration are important in ensuring the complete oxidation of contaminants as well as minimizing the amount of active metal leached into the solution [8]. A previous report on CuO nanosheets as a Fenton-like catalyst showed that at pH 9 around 10 ppm Cu leached into the solution, with over 20 ppm leached at pH 3 [11]. Similarly, CuO supported on CeO2 used at pH 5 showed 9% of the Cu loading leaching into the solution, which has significant implications for such catalyst reusability [18]. Solution pH is the chief parameter affecting metal leaching since heterogeneous catalysts tend to dissolve at lower pH values but remain stable as the pH increases. Adding an external base can help regulate pH, but recent work on Fe-doped MgO nanoparticles as a photo-Fenton-like catalyst showed that such a bifunctional catalyst can provide the active site for ROS generation while regulating pH via surface dissolution with high conversion and no metal leaching [19]. Furthermore, Fenton-like reactions occurring in basic pH have been shown to have contributions from both •OH and HO2 • / •O2 radical species that are generated from Fe and Mn-based catalysts [16,19,20]. Therefore, basic conditions provide a suitable process condition where fast reaction kinetics can be attained with a lower risk of leaching the active metal, which would require downstream metal removal, increasing process cost, and complexity.

Mesoporous MgO nanoparticles have been shown to exhibit superior intraparticle diffusion properties compared to the bulk counterparts in adsorption reactions [21-24], and have been shown to facilitate fast kinetics in Fenton-like reactions [19]. MgO is also a low solubility basic support that is utilized to raise the solution pH [25,26]. This study reports the use of Cu-doped MgO nanoparticles as a photo-Fenton-like catalyst for the oxidation of salicylic acid (SA), an ingredient in non-steroidal anti-inflammatory drugs (NSAIDs), and tetracycline (TCL), an antibiotic molecule prevalent in wastewater [27,28]. SA and TCL have been detected in concentrations up to 27 ppm and 32 ppm in various wastewater streams [28,29]. This study discusses catalyst synthesis and characterization, reaction kinetics and effects of process parameters, mechanistic insights from quenching experiments and possible reaction pathways, as well as post-reaction catalyst characterization to elucidate electronic structural changes that are induced in the active site by the Fenton-like reaction.

2. Experimental methods

2.1. Mesoporous Cu-MgO nanoparticle synthesis

A previously developed facile, thermal decomposition procedure was modified and used to synthesize 2.5%, 5%, and 10% (by weight) CuMgO [22,30]. Briefly, a solution of Mg(NO₃)₂·6H₂O (MilliporeSigma, 99%) and Cu(NO₃)₂·3H₂O (Sigma, 99 +%) was prepared in methanol with the required mass ratios and a 0.59 M NaOH/methanol solution was added dropwise under the reflux temperature of 65 °C. After 30 min of reaction at reflux temperature, the resulting precipitate was collected by centrifugation, washed three times using a 1:1 ratio of ethanol/water solution and dried at 80 °C overnight. The dry solid was calcined at 450 °C for 2 h (2 °C/min ramp rate) in static air. Next, 0.5 g of the prepared catalyst was added to 40 mL deionized water and stirred for 12 h. After stirring, the gel was separated by centrifugation and dried at 80 °C. The sample was then calcined at 450 °C for 2 h (2 °C/min ramp rate) in static air to obtain the final catalyst.

2.2. Catalyst physicochemical characterization methods

2.2.1. Powder X-ray diffraction (XRD)

The crystal structure of all catalysts was confirmed using powder X-ray diffraction (Empyrean, PANalytical B.V.). The applied current was 40 mA and the applied voltage was 45 kV. The X-ray mirror that was used was a graded, flat Bragg-Brentano HD mirror, with the step size set to 0.0131 degrees.

2.2.2. N₂ physisorption

 N_2 physisorption was used to measure surface area using a Micromeritics ASAP2020 surface area and porosimetry system. Samples were degassed at 250 $^\circ\text{C}$ before analysis.

2.2.3. Atomic absorption spectroscopy (AAS)

Perkin-Elmer AAnalyst200 AAS was utilized with an air-acetylene flame to measure copper concentrations in aqueous solutions. A 1000 ppm Cu standard solution from PerkinElmer was used to prepare calibration standards.

2.2.4. Mass spectrometry (MS)

A Micromass Quattro Micro API (Micromass UK LTD) was used for mass spectral characterization of the reaction solution. A Waters Alliance HPLC pump, column heater, and autosampler were used for sample injection. SA was scanned in negative mode, while TCL was scanned in positive mode.

2.2.5. X-ray photoelectron spectroscopy (XPS)

XPS analysis was carried out with a ULVAC-PHI VersaProbe III instrument using a monochromatized Al K α X-ray source (1486.6 eV). The pass energy of the analyzer was 55.5 eV, the acquisition area had a diameter of 100 μ m, and the scan step size was 0.1 eV. Binding energies were corrected for charging by referencing the C 1 s peak at 285.0 eV. Atomic concentrations were calculated from the areas under individual high-resolution XPS spectra using manufacturer-provided sensitivity factors. CasaXPS was used for spectra manipulation and quantification [31].

2.2.6. High-angle annular dark-field scanning transmission electron microscopy with energy dispersive X-ray spectroscopy, and high-resolution transmission electron microscopy (HAADF-STEM/EDS and HR-TEM)

HAADF STEM/EDS was used to confirm dopant distribution. A Scanning Transmission Electron Microscope (FEI Talos 200x) equipped with a four-quadrant 0.9-sr spectrometer was used for elemental and compositional mapping. HRTEM imaging was used to study the nanocrystals and was performed on a JEOL2100F operating at 200 kV.

2.2.7. Ultraviolet-visible diffuse reflectance (UV-vis DR)

UV–vis DR spectra were obtained using an Agilent Cary Series 5000 UV–vis–NIR spectrophotometer employing an integration sphere diffuse reflectance attachment (Harrick Praying Mantis Attachment, DRA-2). The sample was loaded as a powder (~20 mg) into an in situ environmental cell (Harrick, HVC-DR2 with a CaF2 window). Each spectrum was taken from 200 to 800 nm. MgO was used as a standard for background absorbance, and the edge energies (E_g) were calculated using a Microsoft Excel Macro spreadsheet. All measurements were collected under ambient conditions. The UV–vis spectra were processed with Microsoft Excel software, consisting of calculation of the Kubelka-Munk function, $F(R_\infty)$, which was extracted from the UV–vis DRS absorbance. The edge energy (Eg) for allowed transitions was determined by finding the intercept of the straight line in the low-energy rise of a plot of $[F(R^\infty)$ $h\nu]^{1/n}$, where n=0.5 for the direct allowed transition, vs $h\nu$, where $h\nu$ is the incident photon energy [32,33].

2.3. Photocatalytic degradation experiments

The SA and TCL solutions were prepared by dissolving SA (Acros Organics, 99+%) and TCL (Alfa Aesar, 91+%) in deionized water (Millipore). The concentrations for SA and TCL were chosen to be consistent with previous literature reports discussing their presence in wastewater streams [28,34,35]. A glass vessel containing 100 mL of SA solution was used in all experiments. The vessel was then exposed to a 350 W Xenon lamp (Newport), which provided an illumination intensity of approximately 100 mW cm^{-2} . 1 mL of solution was periodically filtered with a $0.22 \,\mu\text{m}$ membrane and measured immediately with UV–vis to quantify the SA concentration and HPLC to quantify TCL concentration. Absorbance measurements were collected using a UV–vis $2600 \,\text{spectrophotometer}$ equipped with an ISR- $2600 \,\text{-Plus}$ integrating sphere attachment (Shimadzu). The rates of SA and TCL degradation were defined by the first-order rate equation [36] shown by Eq. (3)

$$C(t) = C_0 e^{-kt} \tag{3}$$

The rate constant k (min $^{-1}$) in Eq. (3) is the first-order rate constant for the degradation of SA and TCL. The initial kinetics were calculated using the 0–15 min time range. The experiments were conducted in triplicate wherever error bars are shown. The quenching experiments were conducted using $^{\bullet}$ OH radical scavenger tert-butanol (TBA, Millipore-Sigma) and $\mathrm{HO_2}^{\bullet}/^{\bullet}\mathrm{O_2}^{-}$ radical scavenger chloroform (CHCl $_3$, Millipore-Sigma). Both quenching agents were used in a 50 mM concentration. The simulated wastewater with inorganic buffering ions was prepared as shown in Table 1 to assess the effect of buffering on the kinetics of the Cu-MgO catalyst. The ion concentrations were selected from the previously reported simulated wastewater composition [37].

Table 1
Concentrations of ionic species for simulated synthetic wastewater.

Component	Concentration (M)
Na ⁺	0.13
Cl ⁻	0.010
NO ₃	0.0059
HCO3-	0.018
CO ₃ ² - SO ₄ ² -	0.018
SO ₄ ²⁻	0.031

3. Results and discussion

3.1. Catalyst crystal structure characterization

The crystal structure of the synthesized Cu-MgO catalysts was characterized using powder XRD. The major diffraction peaks for the MgO structure are present in all three catalysts as shown in Fig. 1a [22]. As shown in Fig. 1b, the presence of additional minor peaks in 2.5% and 5%, as well as major peaks in 10% Cu-MgO can be observed. These peaks were compared to a reference CuO pattern and confirmed to be due to the presence of CuO nanoparticles [38]. As Cu weight increases, the CuO $(0\ 0\ 2), (-1\ 1\ 1), (1\ 1\ 1),$ and $(2\ 0\ 0)$ peak intensities increase, indicating the formation of nanoparticles that increase in domain size with the higher loading. The slight shift in the MgO (1 1 1) peak is attributed to the solid solution formation between MgO and CuO, which occurs due to the similar ionic radii of Mg^{2+} and $Cu^{\overline{2}+}$ (0.072 and 0.073 nm, respectively) facilitating the dissolution of Cu²⁺ into the MgO lattice [22,39, 40]. N₂ physisorption was used to measure the specific surface area and pore volume. The N₂ physisorption isotherms shown in Fig. 1c indicated the type IV shape specific to mesopore structure. Table 2 shows the resulting surface areas and pore volumes measured from N₂ physisorption. It can be seen that high surface area nanoparticles were synthesized in each case. The increasing Cu loading led to lower surface areas due to the low surface area of CuO clusters.

HAADF-STEM/EDS was used to study the Cu dispersion over the MgO nanoparticles. Fig. 2a–c show the STEM/EDS maps for 2.5%, 5%, and 10% Cu-MgO catalysts. In all three cases, a variety of CuO particle sizes are evident due to the uneven dispersion. Fig. 2d-f shows the HR-TEM results for the Cu-MgO catalysts. In each catalyst the p-spacing measurements show select CuO facets as indicated in Fig. 2d–f, agreeing with the XRD observations showing that CuO nanoparticles are present on the MgO support. The CuO (1 1 1), (1 1 0), (-1 1 1), (0 0 2), and (1 1 2) p-spacings were measured to be 0.233–0.235 nm, 0.277 nm, 0.254–0.257 nm, 0.253 nm, and 0.179 nm, respectively, and were found to be in agreement with previous literature values for CuO [41–43]. Fig. 2g–i show the morphology for the particles in HR-TEM. For all three loadings needle-like particles are present.

Table 2The BET surface areas and pore volumes for Cu-MgO nanoparticles.

Catalyst	Surface area (m ² /g)	Pore volume (cm ³ /g)
2.5% Cu-MgO	205	0.74
5% Cu-MgO	170	0.97
10% Cu-MgO	169	0.76

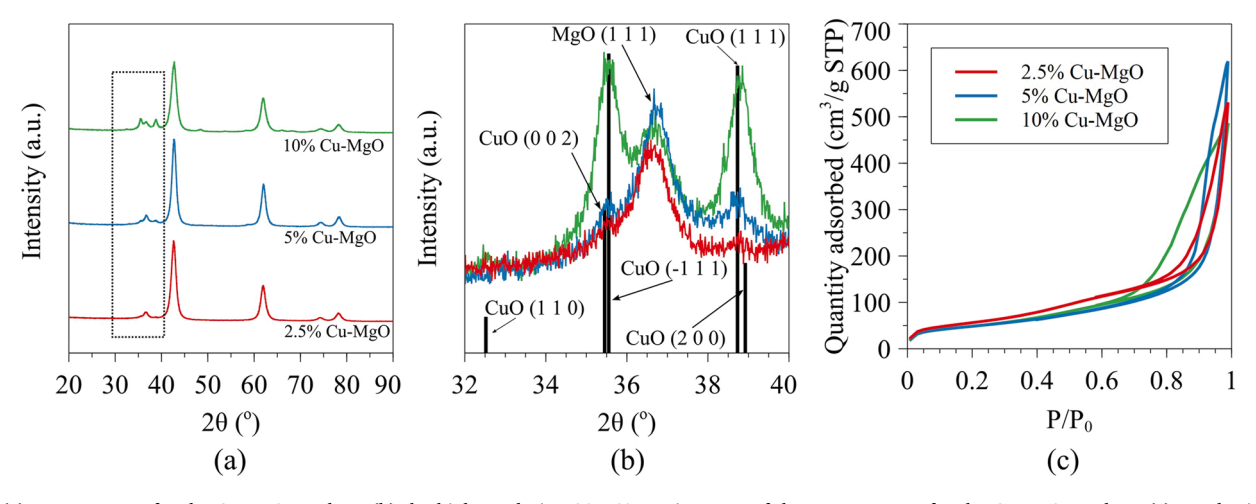


Fig. 1. (a) XRD patterns for the Cu-MgO catalysts (b) the high resolution 32° - 40° region scan of the XRD patterns for the Cu-MgO catalysts (c) N_2 physisorption isotherms for the as-synthesized Cu-MgO catalysts.

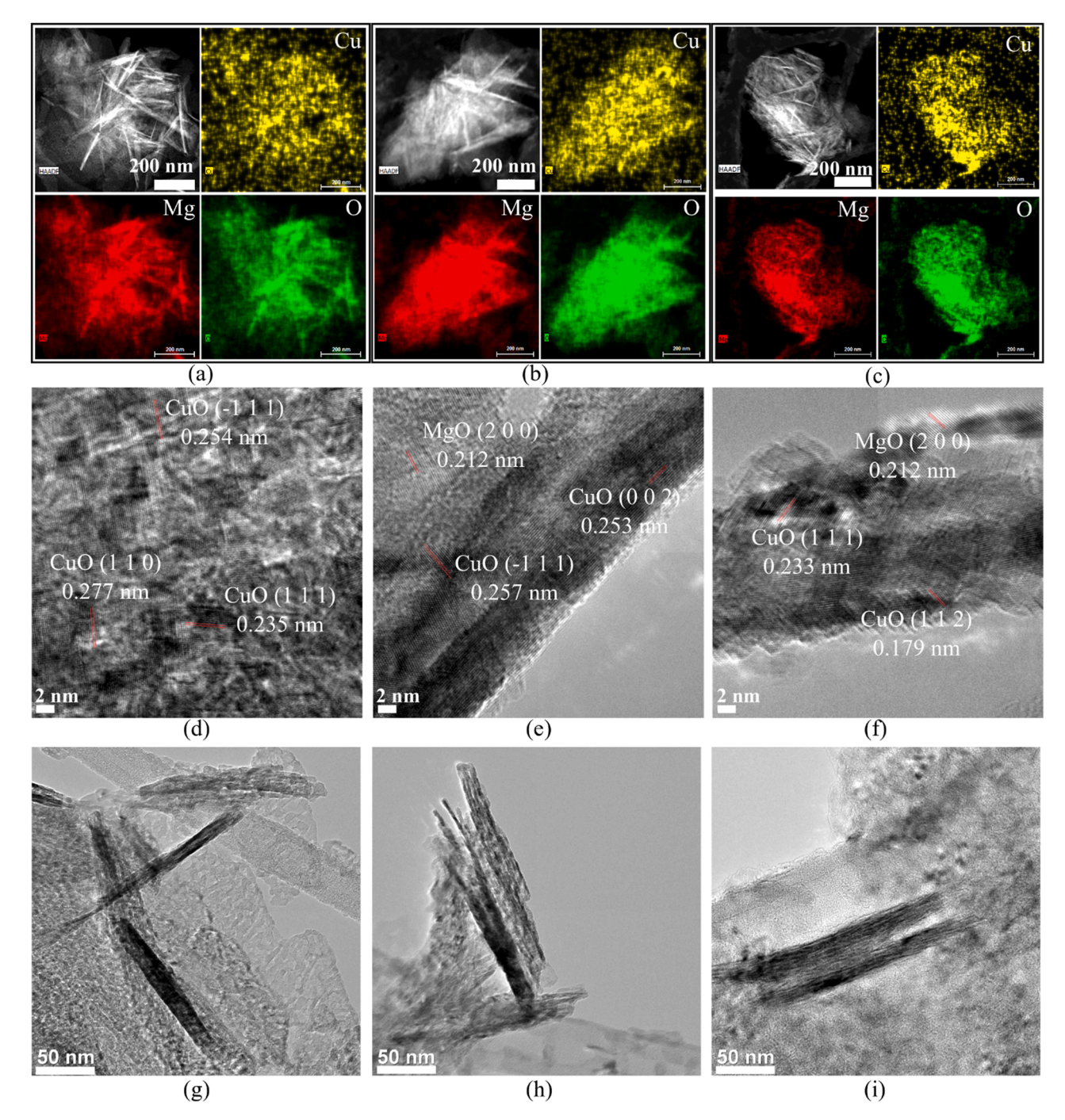


Fig. 2. HAADF-STEM/EDS data of (a) 2.5% Cu-MgO (b) 5% Cu-MgO (c) 10% Cu-MgO. HR-TEM with measured p-spacings of (d) 2.5% Cu-MgO (b) 5% Cu-MgO (f) 10% Cu-MgO. HR-TEM showing morphology of (g) 2.5% Cu-MgO (h) 5% Cu-MgO (i) 10% Cu-MgO.

3.2. Electronic and molecular structure characterization

UV–vis analysis of the as-synthesized Cu-MgO catalysts provided insights into the coordination and oxidation state information of the Cu active sites. The ligand-to-metal charge transfer (LMCT) band for all three Cu-MgO catalysts is centered around 275 nm as shown in Fig. 3a. This transition corresponds to the electron transfer from the oxygen ligand in the photoreduction required to initiate the fast step of the Fenton-like reaction [44,45]. This value is typical for octahedrally coordinated ${\rm Cu}^{2+}$ species [46,47]. The bandgaps for the 2.5%, 5%, and 10% Cu-MgO catalysts were calculated to be 3.0 eV, 3.0 eV, and 2.8 eV, respectively. The slightly lower bandgap of 10% Cu-MgO is attributed to having more Cu-O-Cu polymeric units due to the higher loading, as

having more bridging bonds leads to a lower bandgap [48]. The d-d transfer bands for the Cu-MgO catalysts appear as broad peaks in the 360–600 nm region. [49] XPS was used to study the oxidation state of Cu in the surface region. The XPS results shown in Fig. 3b further confirm the presence of Cu²⁺ in all catalysts, with all three samples exhibiting a Cu $2p_{3/2}$ peak centered around 934.9 eV and a Cu $2p_{1/2}$ peak centered around 954.8 eV which agree with previous studies on CuO/MgO [50]. Additionally, the characteristic shakeup peaks are centered around 942.7 eV and 962.7 eV, which agree with previously reported values [51,52].

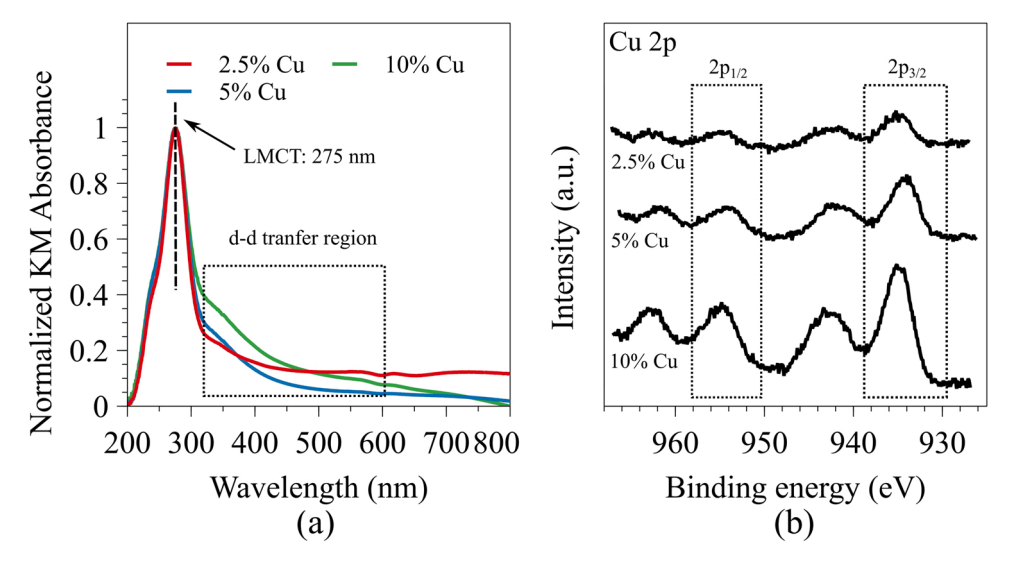


Fig. 3. (a) UV-vis DR spectra (b) Cu 2p region obtained using XPS.

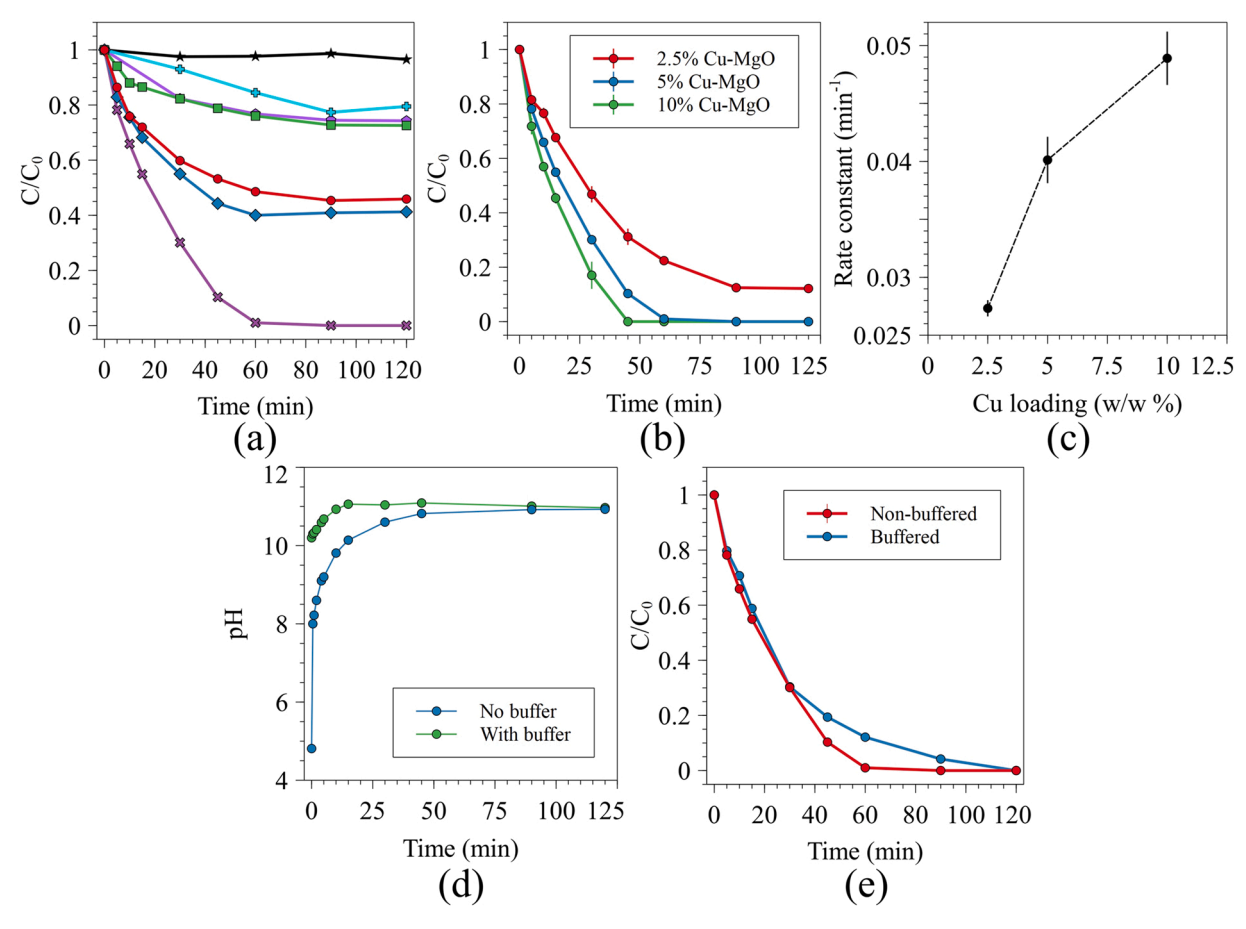


Fig. 4. (a) \bigstar – 50 ppm SA under light (with no catalyst and no H_2O_2), \clubsuit - 50 ppm SA + 20 mM H_2O_2 under light (no catalyst), \blacksquare - 500 ppm undoped MgO + 50 ppm SA in dark (no H_2O_2), \spadesuit - 500 ppm Cu-MgO + 50 ppm SA in dark (no H_2O_2), \spadesuit - 500 ppm Cu-MgO + 50 ppm SA under light (no H_2O_2), \spadesuit - 500 ppm Cu-MgO + 50 ppm SA + 20 mM H_2O_2 in dark, x - 500 ppm Cu-MgO + 50 ppm SA + 20 mM H_2O_2 under light (b) Relative concentration of SA for Cu-MgO catalysts (500 ppm catalyst, 50 ppm SA, 20 mM H_2O_2) (c) The rate constant as a function of Cu loading on MgO (500 ppm catalyst, 50 ppm SA, 20 mM H_2O_2) (d) The solution pH during reaction for 500 ppm 5% Cu-MgO reacted with 50 ppm SA and 20 mM H_2O_2 (both buffered and non-buffered) (e) The relative concentration of SA for buffered and non-buffered experiments.

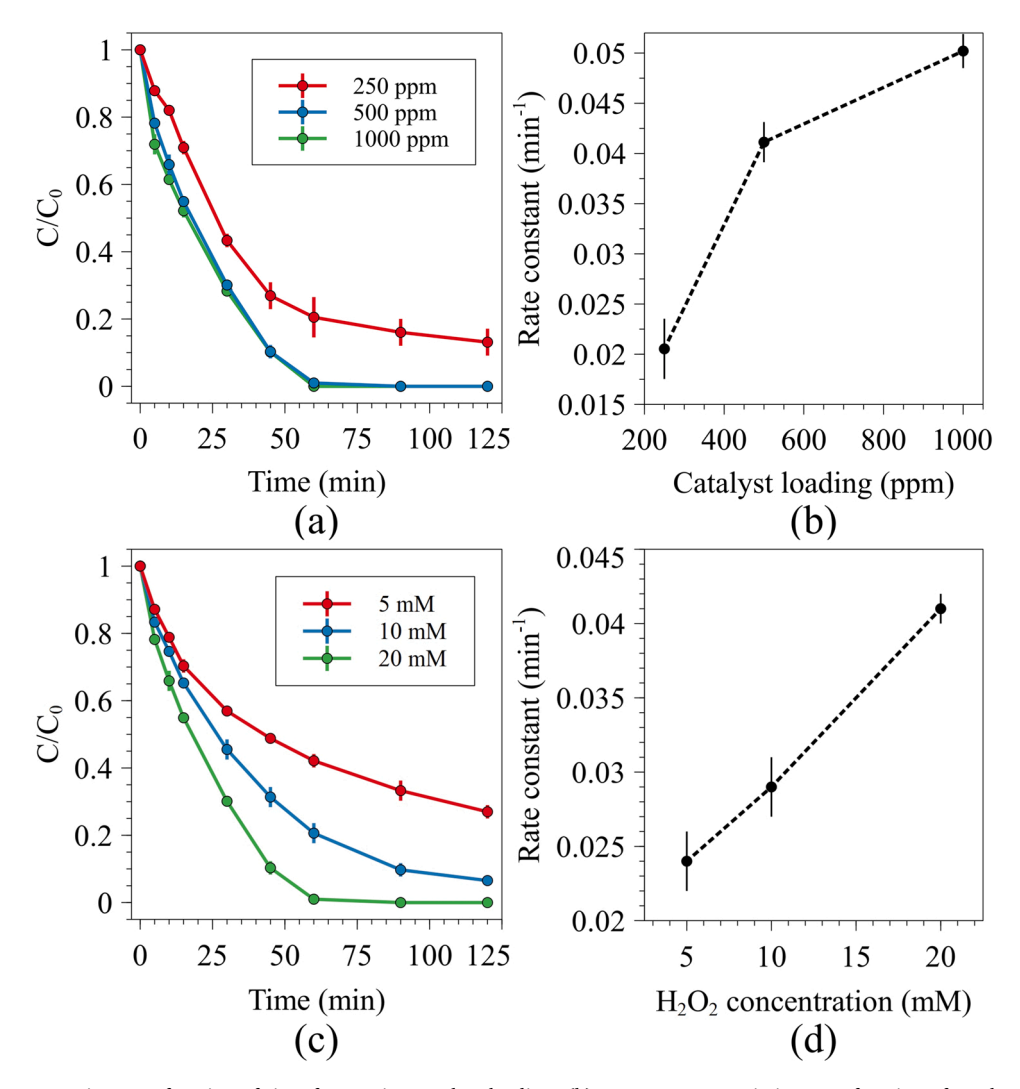


Fig. 5. (a) Relative concentration as a function of time for varying catalyst loadings (b) Rate constant variation as a function of catalyst loading (50 ppm SA, 20 mM H_2O_2) (c) Relative concentration as a function of time for varying H_2O_2 concentrations (d) Rate constant variation as a function of H_2O_2 concentration (50 ppm SA, 500 ppm 5% Cu-MgO).

3.3. Photo-Fenton-like degradation of salicylic acid (SA) and tetracycline (TCL)

The SA degradation kinetics were studied by fitting the initial reaction data to the first-order equation shown in Eq. 3. Control experiments were conducted to verify that the photo-Fenton-like reaction is occurring with the Cu-MgO catalyst. Fig. 4a summarizes the results of these control experiments. To investigate whether light alone can degrade SA, 50 ppm SA was exposed to the light source with no other reactants. No degradation was observed by light without other reactants. When exposed to light in the presence of H₂O₂, a 20% reduction of concentration was observed but this reduction is attributed to the wet oxidation of SA that results in the production of quinones and catechols [53]. Since wet oxidation does not lead to complete conversion as desired in water treatment, the catalyst becomes a required component of the process to achieve full oxidation. To assess the effect of the MgO support, 50 ppm SA was mixed with 500 ppm of undoped MgO, which led to 28% removal of SA via adsorption. Furthermore, the effect of light on the photo-Fenton-like reaction was tested by reaction 500 ppm Cu-MgO, 50 ppm SA, and 20 mM H₂O₂ in the dark. The resulting change in

relative concentration over time was shown to be similar to the reaction of 500 ppm Cu-MgO and 50 ppm SA with no H₂O₂, indicating the light is required for the reaction to occur. The effect of Cu loading on MgO was investigated to determine an optimal Cu loading. As shown in Fig. 4b, the 2.5% Cu-MgO leads to 80% conversion within 2 h of reaction, while 5% and 10% Cu-MgO reach complete conversion within 60 min and 45 min, respectively. Fig. 4c shows the calculated initial rate constant as a function of Cu loading. A monotonic increase in rate constant is observed as the Cu loading is increased to 2.5%, 5%, and 10%. Finally, Fig. 4d shows the pH of the solution as a function of time during the reaction. The starting pH for the SA solution is 4.8. The MgO surface dissolution rapidly increases the pH from 4.8 to 8 within 30 s and reaches a stable pH in the range of 10.8–11 within 45 min. This increase in pH due to MgO dissolution has been reported in previously published adsorption literature [25,54]. MgO is a largely insoluble support, but surface hydration, which is caused by water diffusing into the pore structure, leads to MgO dissolution and subsequent Mg(OH)2 formation [25]. This rapid pH increase is followed by a stabilization of pH, which occurs due to Mg(OH)2 precipitation covering the MgO surface, which terminates hydration [25,55]. This allows for a stable pH to be

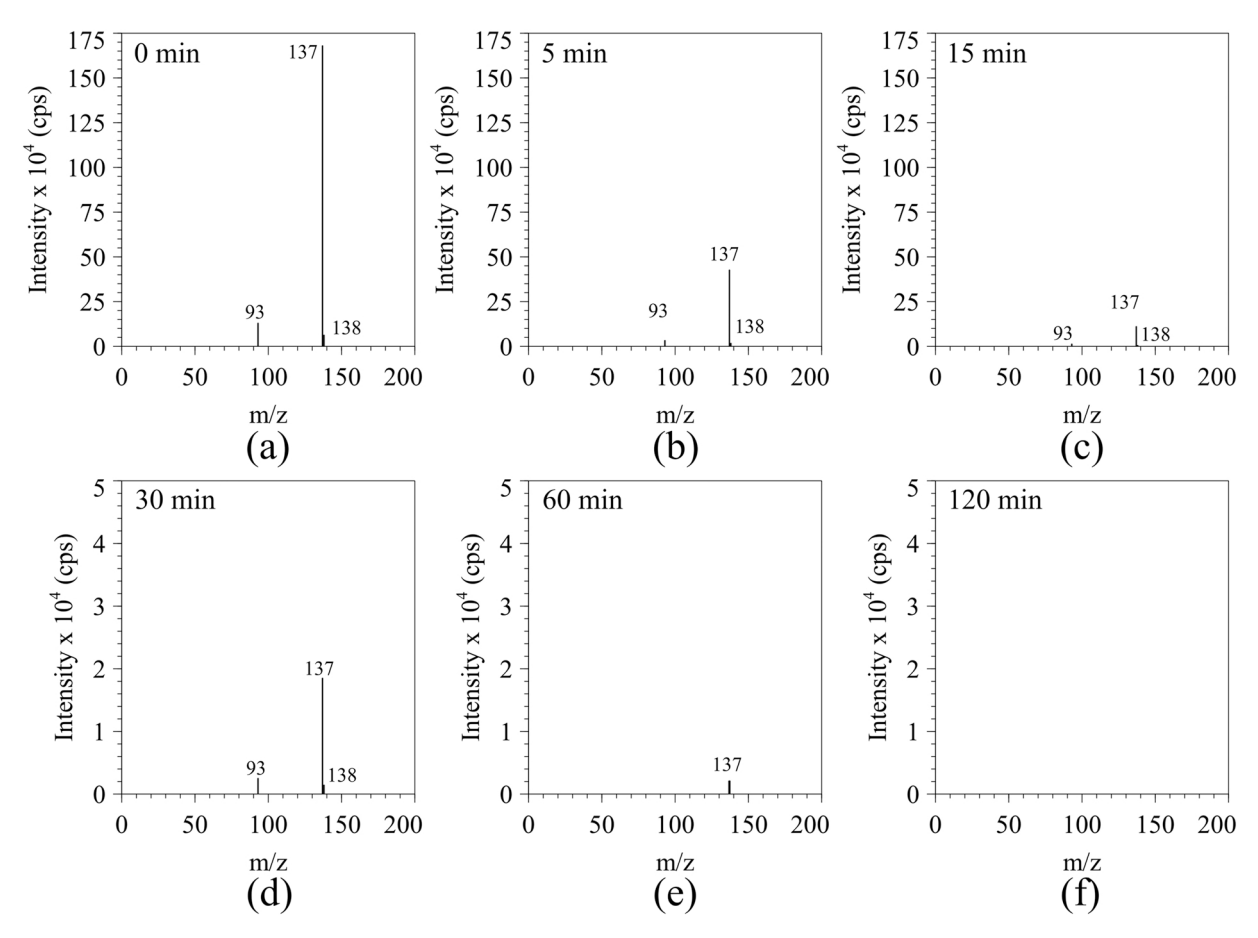


Fig. 6. Time-resolved mass spectra for 50 ppm SA reacted with 500 ppm 5% Cu-MgO and 20 mM H₂O₂.

maintained without further pH increase, although over time, $\rm CO_2$ dissolution from the atmosphere can lead to a slight depression of the pH [25]. The resulting aqueous phase was sampled after 5, 10, and 15 min and no Cu was detected in the solution using AAS. Similarly, no Cu was detected in the aqueous phase at the end of the first and fifth reaction cycles. The basic pH prevents Cu from dissolving out of the catalyst, as similar behavior has been reported in reducing catalyst leaching at basic pH operating conditions [11,19]. Furthermore, the effect of buffering caused by inorganic ions commonly present in wastewater was tested by performing the reaction in simulated wastewater, with the composition previously shown in Table 1. The reaction kinetics were slightly slower in the initial 15 min, with the rate constant decreasing to 0.036 min $^{-1}$ in the buffered case compared to 0.042 min $^{-1}$ in the non-buffered case (Fig. 4e). The buffered solution showed an initial pH of 10.2, which increased over 2 h to 10.94 (Fig. 4d).

Since 5% Cu-MgO yields complete conversion within 1 h, the subsequent parameter variation with $\rm H_2O_2$ and catalyst loading was conducted using this catalyst. Fig. 5a shows the relative concentration as a function of time for 250 ppm, 500 ppm, and 1000 ppm catalyst loadings. Fig. 5c shows the relative concentration variation over time for 5 mM, 10 mM, and 20 mM $\rm H_2O_2$ concentrations. The 5 mM $\rm H_2O_2$ concentration leads to 73% conversion of SA, while 10 mM and 20 mM concentrations lead to 94% and 100% conversion in 2 h.

Time-resolved MS was used to study whether complete conversion of SA can be achieved. At time 0 before the addition of the catalyst and H_2O_2 , the parent SA peaks are observed at m/z values of 93, 137, and 138. At 60 min only a minor peak of 137 was present in the spectrum,

while at 120 min no SA peaks are present. Additionally, no intermediates are present in the final solution, indicating that SA was completely oxidized to CO_2 and H_2O . (Fig. 6).

Another common pharmaceutical molecule prevalent in wastewater, the antibiotic tetracycline was subjected to the same experimental conditions as SA (500 ppm 5% Cu-MgO, 20 mM $\rm H_2O_2$, 25 ppm TCL). As shown in Fig. 7a, within the first 10 min of reaction the TCL, as measured using HPLC, was almost completely reacted, but the presence of several intermediate peaks was observed in Fig. 7b. While 20 mM H₂O₂ was sufficient to oxidize the smaller one-ring molecule SA, the four-ring structure of TCL was shown to require stronger oxidizing conditions to completely degrade. While TCL remediation can be achieved under 2 h (evidenced by the lack of parent TCL peaks in the final mass spectrum) with one initial dose of H₂O₂, complete oxidation was not achieved in this scenario. The H2O2 is consumed due to deprotonation under alkaline conditions and thus, the initial injection of H₂O₂ may not be sufficient to degrade the larger TCL molecule compared to SA [34]. However, by utilizing several H₂O₂ doses delivered at multiple time points, the intermediate distribution was significantly changed. Fig. 7c shows the TCL concentration for the reaction with 500 ppm Cu-MgO, 25 ppm TCL, and 3 doses of 20 mM H₂O₂ reacted for 2 h. In this case, the TCL is completely removed as well, but the number of intermediate peaks in the time-resolved MS analysis in Fig. 7d is significantly lower. The case with one H₂O₂ injection in the beginning led to 63 mass spectral peaks being present in the final solution (after 120 min), while the case with 3 separate H_2O_2 injections only led to 7 mass spectral peaks in the final solution. This significant reduction of MS

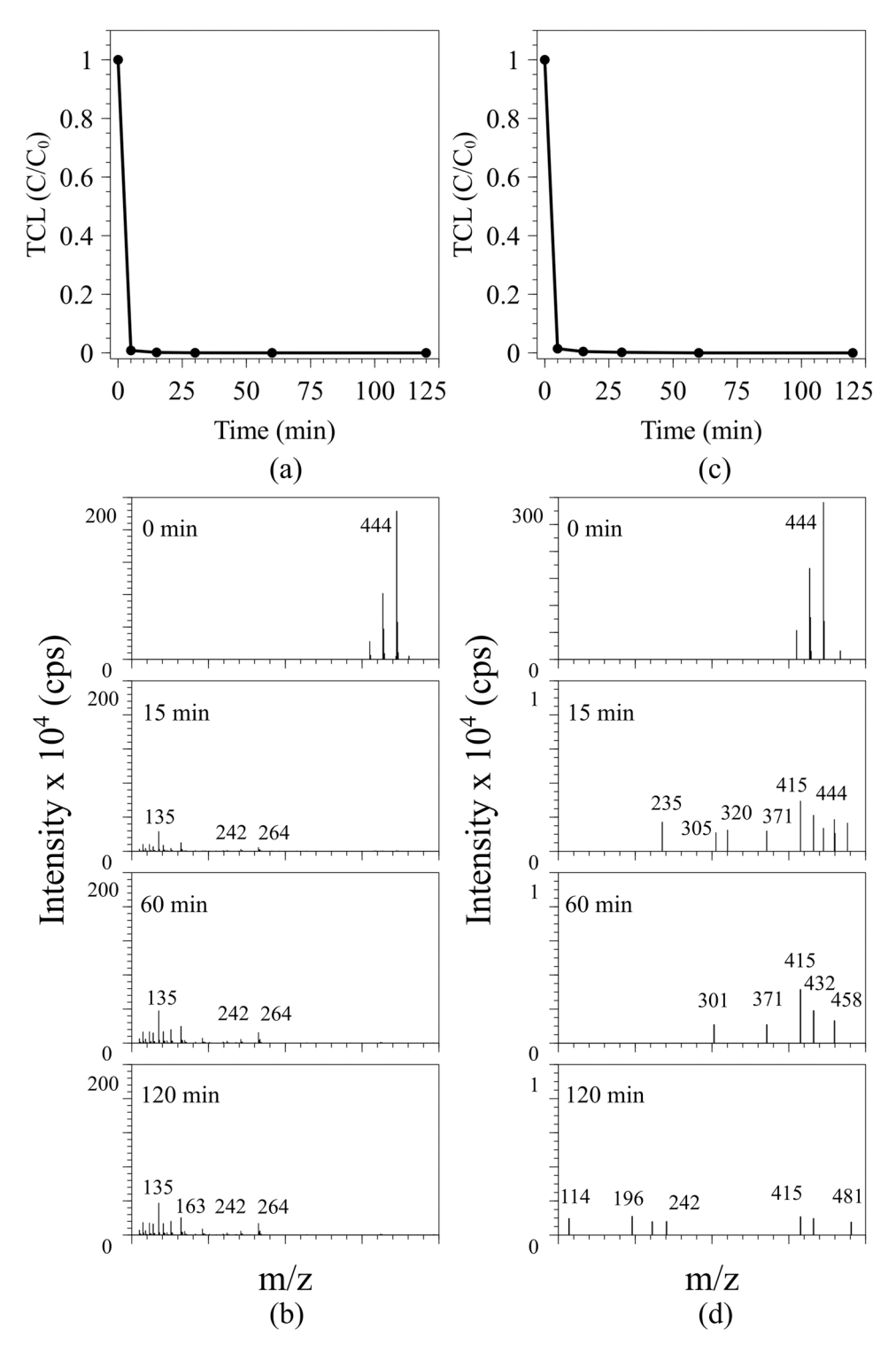


Fig. 7. (a) TCL concentration as a function of time (measured using HPLC) (b) Time-resolved mass spectra for 25 ppm TCL (reacted with 500 ppm 5% Cu-MgO, 25 ppm TCL, 20 mM H_2O_2 1 dose at t=0 min) (c) TCL concentration as a function of time (d) Time-resolved mass spectra for 25 ppm TCL (reacted with 500 ppm 5% Cu-MgO, 25 ppm TCL, 60 mM H_2O_2 as 3 \times 20 mM doses at t=0, 15, 60 min).

peaks indicates that the number of intermediate species present after the reaction with 3 $\rm H_2O_2$ injections leads to more efficient degradation of a larger molecule such as TCL.

The inorganic ions released during the reaction with TCL were measured using ion chromatography. The surface dissolution of MgO led to the release of Mg $^{2+}$, with a final concentration of 40.7 ppm (Fig. 8). Specifically, in the case of TCL, the heteroatom N was shown to be liberated in the form of $\mathrm{NH_4}^+$ within the first 5 min and a stable

concentration of $\mathrm{NH_4}^+$ was observed from that 5-minute time point onward as shown in Fig. 8. This is consistent with previously published degradation pathways, where heteroatoms present in emerging contaminants are converted to inorganic ions [34,56].

By examining time-resolved MS spectra and comparing them to previous literature on tetracycline degradation using various Fenton-like catalysts, possible degradation products can be identified (Fig. 9) [34,56–58]. Adding $\rm H_2O_2$ to the TCL solution once at the beginning of

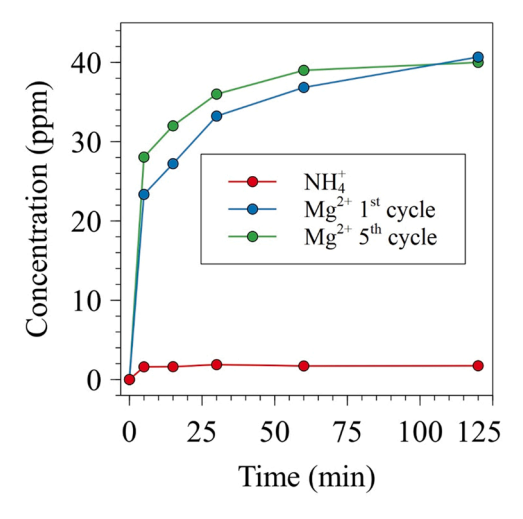


Fig. 8. The concentrations of $\mathrm{NH_4}^+$ and $\mathrm{Mg^{2+}}$ ions during the photo-Fenton-like reaction with TCL and $\mathrm{Cu-MgO}$.

the reaction led to intermediates such as P1, P3, P6, P8, P9-P13, and linear organic acids present in the solution after 2 h of reaction. Previous studies have evaluated the toxicity of the intermediate products formed during TCL degradation using the Toxicity Estimation Software Tool (TEST) based on quantitative structure-activity relationships (QSAR) [34,59]. These studies show that P10 and P11 products can be classified as "developmental non-toxic" while P9 saw a significant decrease in toxicity compared to TCL [34]. Due to the short lifetimes of the ROS involved in the degradation, a semi-continuous H₂O₂ dosing strategy is more effective for achieving full mineralization [60]. As discussed previously, the number of intermediate molecules can be significantly reduced by introducing multiple H₂O₂ doses at various time points. Compared to only one H₂O₂ dose, the multiple doses resulted in only P2, P8, and fumaric acid being present from the original distribution of intermediates. New peaks were detected at m/z values of 196, 222, 432, and 481, which were also reported in work studying TCL degradation using H₂O₂ without a catalyst and assigned to TCL derivatives such as oxytetracycline [61,62]. Radical recombination can limit the amount of ROS available for the reaction over time, so multiple injections of H₂O₂ can ensure a steady presence of ROS [8]. Therefore, longer reaction times with optimized H₂O₂ delivery are expected to completely remove the smaller intermediate molecules formed during TCL degradation, making the effluent safe for downstream biological treatment and eventual discharge.

The reusability of the photo-Fenton-like Cu-MgO catalyst was studied by performing five catalytic cycles on the 5% Cu-MgO catalyst as shown in Fig. 10a. While the SA is almost completely oxidized in 1 h during the first catalytic cycle, subsequent cycles require more time for complete oxidation, with the 5th cycle leading to 96% conversion. In the case of TCL, the parent TCL molecule is completely degraded in all runs with a single H₂O₂ injection but intermediate products are observed in the solution after 2 h. The minor losses in initial rate and overall conversion can be attributed to Cu-sites agglomerating. To support this argument, XRD patterns of the post-reaction catalysts are shown in Fig. 10b. The asterisk (*) denotes Mg(OH)₂ peaks while the circle (o) denotes the CuO peaks. The MgO peak intensities reduce due to the loss of crystallinity caused by surface dissolution, which further leads to the formation of Mg(OH)₂. The cluster of peaks in the 2θ range of 32°-40° broadens, indicating amorphization. While Cu-site agglomeration and support amorphization are evident in post-reaction characterization, the

catalyst activity is retained with minor loss over 5 cycles, indicating that the catalyst reusability is satisfactory.

3.4. Fenton-like reaction induced catalyst structural and active site changes

The UV-vis DR spectra for the post-reaction Cu-MgO catalysts are shown in Fig. 11a. The bandgaps for post-reaction 2.5%, 5%, and 10% Cu-MgO catalysts were 2.9 eV, 2.9 eV, and 2.7 eV, respectively. The reduction in bandgap indicates that more Cu-O-Cu bonds are present in the post-reaction sample, which shows that Cu sites have undergone agglomeration as discussed in Section 3.3 with XRD analysis. Furthermore, the UV-vis DR results show a shift of the LMCT band from 275 nm to higher energy at 259 nm, which indicates that in addition to the octahedrally coordinated Cu²⁺ species, some tetrahedrally coordinated Cu⁺ species may be present, since the Cu⁺ LMCT occurs at higher energy [63]. The cyclic oxidation/reduction that occurs during the photo-Fenton-like reaction is considered to be the reason for the presence of a minor quantity of reducing sites in the post-reaction catalysts. As shown by Eqs. (1) and (2), the ROS generation step with Cu⁺ is two orders of magnitude faster compared to the step where Cu²⁺ reacts to form radicals, showing that Cu⁺ is consumed much faster compared to Cu²⁺, leading to only a small quantity of the less stable Cu⁺ being present in the catalyst sample. Minor shoulders centered around 310 nm and 360 nm appear in the post-reaction samples, and these are attributed to the LMCT bands of various Cu-O-Cu cluster sizes since these oligomeric species with varying sizes and morphologies exhibit a variation in the band position in the 300-360 nm region [47,64]. The XPS spectra for the post-reaction catalysts are shown in Fig. 11b. A prominent change in Cu2p spectral region was the reduction of the shakeup peaks. This reduction in the post-reaction catalysts indicates that in addition to CuO, some Cu(OH)₂ or even Cu₂O may be present following the reaction due to surface hydration and the Fenton reaction [65]. Fig. 11c shows the quantification of Cu in the surface region using the Cu 2p/Mg 2p peak area ratio in the as-synthesized and post-reaction catalysts. In all three cases, a reduction in the Cu 2p/Mg 2p ratio is observed, indicating that Cu sites undergo agglomeration under reaction conditions and form larger nanoparticles. This reduces the number of exposed Cu sites, leading to slightly lower rates during catalyst recycling. The trend of initial rate constant as a function of Cu loading on the catalyst shown in Fig. 4b is consistent with the surface region Cu atomic concentration increase shown in Fig. 11c, as the surface region Cu concentration increases linearly as the Cu loading increases.

3.5. Potential photo-Fenton-like ROS generation mechanism

Selective quenching agents were used to identify whether *OH radicals or $HO_2^{\bullet/\bullet}O_2^{-}$ radicals were more active in the photo-Fenton-like reaction at high pH conditions on the Cu-MgO catalyst surface. Compared to the untreated experiment with no quenching agent, the addition of CHCl₃ led to a significant decrease in the rate constant, while the addition of TBA led to a lesser decrease in the rate constant (Fig. 12a). This indicates that *OH radicals play a role in the reaction mechanism, while the $HO_2^{\bullet/\bullet}O_2^{-}$ radicals play a more dominant role. The types of radical species generated by the Fenton-like catalyst are dependent on the pH of the solution, with the $HO_2^{\bullet/\bullet}O_2^{-}$ radicals becoming more dominant at more basic pH conditions [19,20]. Similar CuFeO₂ catalysts have been shown to also generate a combination of *OH radicals and $HO_2^{\bullet/\bullet}O_2^{-}$ radicals during reaction [34]. A summary schematic depicting the generation of ROS is shown in Fig. 12b.

Fig. 9. Proposed TCL degradation products formed during the photo-Fenton-like reaction with 500 ppm Cu-MgO and one injection of 20 mM H₂O₂.

4. Conclusions

In summary, two emerging pharmaceutical contaminants, salicylic acid and tetracycline, were degraded in an aqueous solution by the novel Cu-MgO photo-Fenton-like catalyst. The Cu-MgO catalysts were shown to have a high BET surface area (169–205 $\rm m^2/g)$ and the presence of CuO nanoparticles was confirmed using HR-TEM, XPS, and UV–vis DRS. The MgO support undergoes surface dissolution and rapidly increases

the solution pH from 4.8 to $\sim \! 11$ in a salicylic acid solution, which prevents Cu from leaching out of the solid phase. SA was completely degraded in 1 h using 5% Cu-MgO with no by-products under optimal conditions (500 ppm Cu-MgO, 20 mM $\rm H_2O_2$, 50 ppm SA), while TCL degradation resulted in intermediate products being present after 2 h due to insufficient $\rm H_2O_2$ utilization. MS findings show possible TCL degradation intermediates, and that the overall toxicity of the parent TCL is lowered. Furthermore, multiple injections of $\rm H_2O_2$ proved to be a

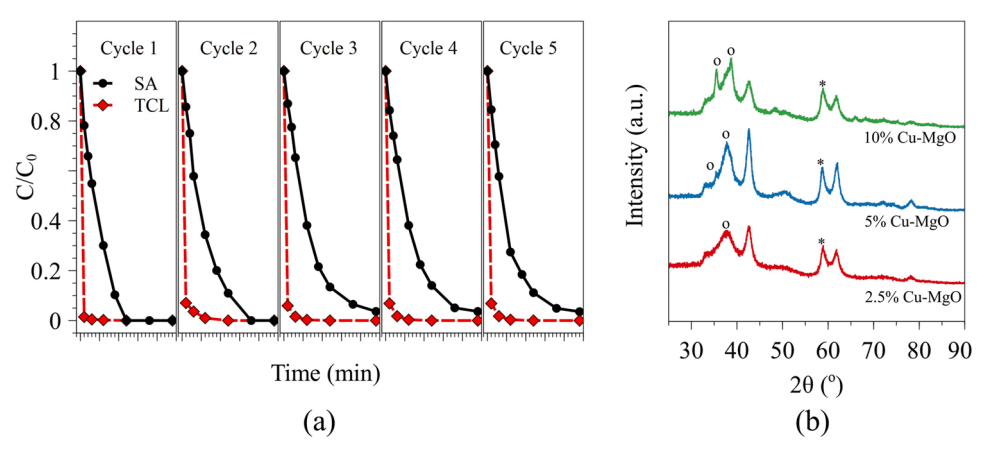


Fig. 10. (a) Recycling experiments for 5% Cu-MgO catalyst (500 ppm catalyst, 50 ppm SA, 20 mM H_2O_2 shown in black, 500 ppm catalyst, 25 ppm TCL, 20 mM H_2O_2 shown in red) (b) XRD pattern for the post-reaction catalyst.

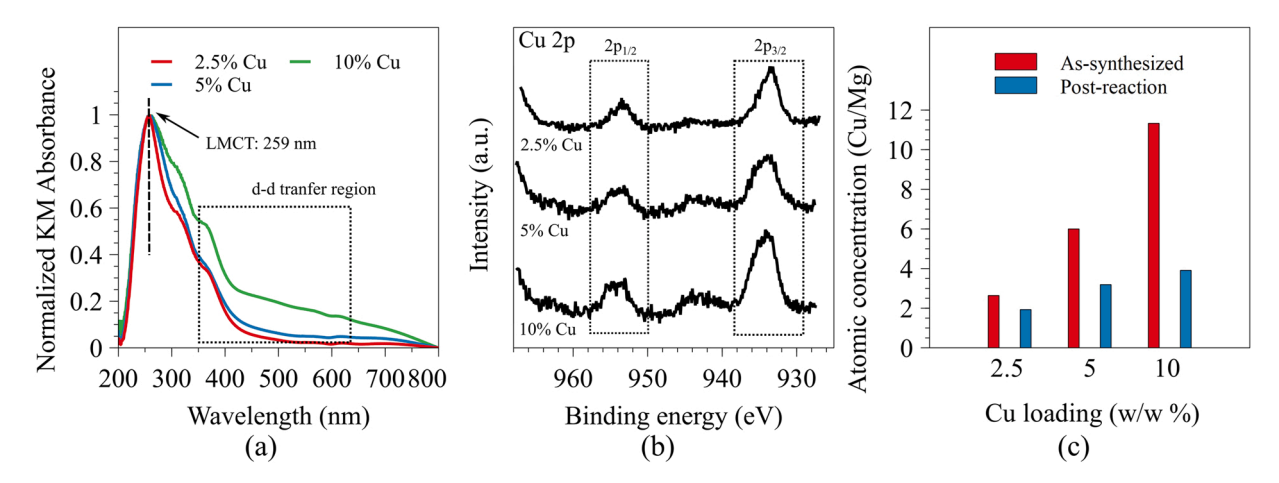


Fig. 11. UV-vis DR spectra for post-reaction catalysts (b) XPS spectra for post-reaction catalysts (c) Cu 2p/Mg 2p peak area ratio for as-synthesized and post-reaction catalysts.

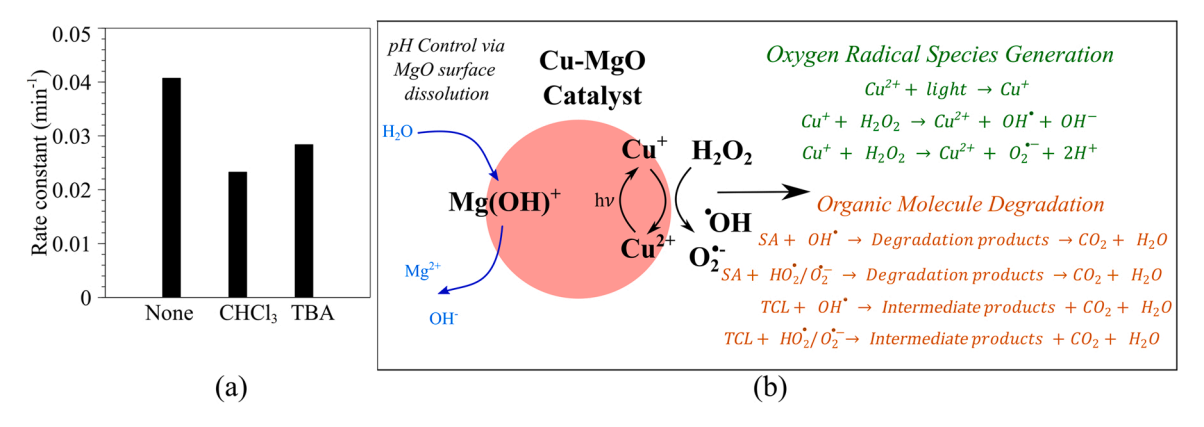


Fig. 12. (a) The rate constant for 500 ppm 5% Cu-MgO reacted with 20 mM H_2O_2 and 50 ppm SA with and without quenching agents (b) Possible ROS generation mechanism based on radical quenching studies.

better treatment strategy for minimizing the number of degradation products of TCL. Characterization using UV–vis DRS and XPS shows that Cu^{2+} sites are reduced to Cu^+ during the Fenton redox cycle. The Cu-MgO catalyst was shown to be stable over five cycles, with minimal activity loss. Quenching experiments showed that both ${}^{\bullet}\mathrm{OH}$ radicals or $\mathrm{HO_2}^{\bullet}/{}^{\bullet}\mathrm{O_2}^{-}$ radicals were formed during the reaction, with the latter species having a larger contribution toward the degradation of SA. These findings show that Cu-MgO can act as a novel photo-Fenton-like catalyst

that operates in a higher pH regime which prevents Cu leaching into the aqueous phase but retains fast kinetics of degradation.

CRediT authorship contribution statement

M.S.: Conceptualization.
M.S., A.K., L.Z., J.P.B.: Investigation.
M.S.: Visualization.
M.S., J.B.: Writing – original draft.
M.S., J.B.: Writing – review & editing.
C.W., L.Z., J.P.B.: Resources.
J.B.: Supervision.
J.

B.: Funding acquisition.

Acknowledgements

This material is based upon work supported by the National Science Foundation under Grant No. CHE 1710120. HRTEM and STEM-EDS were carried out on JEOL2100F and FEI Talos 200X at the Center for Functional Nanomaterials, Brookhaven National Laboratory, which is supported by the U.S. Department of Energy, Office of Basic Energy Sciences, under Contract No. DE-SC0012704. The authors acknowledge Prof. Mark Snyder and Mr. Lohit Sharma for assistance with obtaining BET data, Prof. Israel Wachs and Mr. Daniyal Kiani for assistance with obtaining UV–vis-DRS data, and Prof. Steven McIntosh and Mr. John Sakizadeh for assistance in obtaining UV–vis data.

Conflicts of Interest

The authors declare no conflicts of interest.

References

- M.M. Mekonnen, A.Y. Hoekstra, Sci. Adv. 2 (2016), 1500323, https://doi.org/ 10.1126/sciadv.1500323.
- [2] M.A. Shannon, P.W. Bohn, M. Elimelech, J.G. Georgiadis, B.J. Marïas, A.M. Mayes, Nature 452 (2008) 301–310, https://doi.org/10.1038/nature06599.
- [3] J. Qian, X. Gao, B. Pan, Environ. Sci. Technol. 54 (2020) 8509–8526, https://doi. org/10.1021/acs.est/0r01065
- [4] J. Rivera-Utrilla, M. Sánchez-Polo, M.Á. Ferro-García, G. Prados-Joya, R. Ocampo-Pérez, Chemosphere 93 (2013) 1268–1287, https://doi.org/10.1016/j. chemosphere.2013.07.059.
- [5] J.M. Martin, V. Nagarajan-Radha, H. Tan, M.G. Bertram, J.A. Brand, M. Saaristo, D. K. Dowling, B.B.M. Wong, J. Hazard. Mater. Lett. 1 (2020), 100004, https://doi.org/10.1016/j.hazl.2020.100004.
- [6] M. Mezzelani, S. Gorbi, F. Regoli, Mar. Environ. Res. 140 (2018) 41–60, https://doi.org/10.1016/j.marenvres.2018.05.001.
- [7] M. Silva, J. Baltrusaitis, J. Hazard. Mater. Lett. 2 (2021), 100012, https://doi.org/ 10.1016/j.hazl.2020.100012.
- [8] Y. Zhu, R. Zhu, Y. Xi, J. Zhu, G. Zhu, H. He, Appl. Catal. B Environ. 255 (2019), 117739, https://doi.org/10.1016/j.apcatb.2019.05.041.
- [9] S. Hussain, E. Aneggi, D. Goi, Environ. Chem. Lett. 1 (2021) 3, https://doi.org/ 10.1007/s10311-021-01185-z.
- [10] L. Wu, B. Li, Y. Li, X. Fan, F. Zhang, G. Zhang, Q. Xia, W. Peng, ACS Catal. 11 (2021) 5532–5543, https://doi.org/10.1021/acscatal.1c00701.
- [11] M. Fang, R. Zheng, Y. Wu, D. Yue, X. Qian, Y. Zhao, Z. Bian, Environ. Sci. Nano 6 (2019) 105–114, https://doi.org/10.1039/c8en00930a.
- [12] H.J.H. Fenton, J. Chem. Soc. Trans. 65 (1894) 899–910, https://doi.org/10.1039/ CT8946500899.
- [13] A.D. Bokare, W. Choi, J. Hazard. Mater. 275 (2014) 121–135, https://doi.org/ 10.1016/j.jhazmat.2014.04.054.
- [14] S. Hussain, E. Aneggi, S. Briguglio, M. Mattiussi, V. Gelao, I. Cabras, L. Zorzenon, A. Trovarelli, D. Goi, J. Environ. Chem. Eng. 8 (2020), 103586, https://doi.org/ 10.1016/j.jece.2019.103586.
- [15] C. Dai, X. Tian, Y. Nie, H.M. Lin, C. Yang, B. Han, Y. Wang, Environ. Sci. Technol. 52 (2018) 6518–6525, https://doi.org/10.1021/acs.est.8b01448.
- [16] W. Zhao, Z. Wei, X. Zhang, M. Ding, S. Huang, S. Yang, Appl. Catal. A Gen. 593 (2020), 117443, https://doi.org/10.1016/j.apcata.2020.117443.
- [17] L. Chudal, N.K. Pandey, J. Phan, O. Johnson, L. Lin, H. Yu, Y. Shu, Z. Huang, M. Xing, J.P. Liu, M.L. Chen, W. Chen, ACS Appl. Bio Mater. 3 (2020) 1804–1814, https://doi.org/10.1021/acsabm.0c00098.
- [18] J. Zhu, G. Zhang, G. Xian, N. Zhang, J. Li, Front. Chem. 7 (2019) 796, https://doi. org/10.3389/fchem.2019.00796.
- [19] M. Silva, J. Baltrus, C. Williams, A. Knopf, L. Zhang, J. Baltrusaitis, J. Environ. Chem. Eng. 9 (2021), 105589, https://doi.org/10.1016/j.jece.2021.105589.
- [20] H. Lee, H.J. Lee, D.L. Sedlak, C. Lee, Chemosphere 92 (2013) 652–658, https://doi. org/10.1016/j.chemosphere.2013.01.073.
- [21] J. Zhou, S. Yang, J. Yu, Colloids Surf. A Physicochem. Eng. Asp. 379 (2011) 102–108, https://doi.org/10.1016/j.colsurfa.2010.11.050.
- [22] M. Silva, V. Murzin, L. Zhang, J.P. Baltrus, J. Baltrusaitis, Environ. Sci. Nano 7 (2020) 3482–3496, https://doi.org/10.1039/d0en00660b.
- [23] L. Sharma, R. Kakkar, ACS Appl. Mater. Interfaces 9 (2017) 38629–38642, https://doi.org/10.1021/acsami.7b14370.
- [24] M. Silva, J. Baltrusaitis, Environ. Sci. Water Res. Technol. 6 (2020) 3178–3194, https://doi.org/10.1039/D0EW00679C.

- [25] P. Stolzenburg, A. Capdevielle, S. Teychené, B. Biscans, Chem. Eng. Sci. 133 (2015) 9–15, https://doi.org/10.1016/j.ces.2015.03.008.
- [26] D. Kiani, M. Silva, Y. Sheng, J. Baltrusaitis, J. Phys. Chem. C 123 (2019) 25135–25145, https://doi.org/10.1021/acs.jpcc.9b05292.
- [27] H. Dong, X. Yuan, W. Wang, Z. Qiang, J. Environ. Manag. 178 (2016) 11–19, https://doi.org/10.1016/j.jenvman.2016.04.037.
- [28] N.H. Tran, M. Reinhard, K.Y.H. Gin, Water Res. 133 (2018) 182–207, https://doi. org/10.1016/j.watres.2017.12.029.
- [29] J. Hou, C. Wang, D. Mao, Y. Luo, Environ. Sci. Pollut. Res. 23 (2016) 1722–1731, https://doi.org/10.1007/s11356-015-5431-5.
- [30] S.W. Bian, J. Baltrusaitis, P. Galhotra, V.H. Grassian, J. Mater. Chem. 20 (2010) 8705–8710, https://doi.org/10.1039/c0jm01261k.
- [31] N. Fairley, V. Fernandez, M. Richard-Plouet, C. Guillot-Deudon, J. Walton, E. Smith, D. Flahaut, M. Greiner, M. Biesinger, S. Tougaard, D. Morgan, J. Baltrusaitis, Appl. Surf. Sci. Adv. 5 (2021), 100112, https://doi.org/10.1016/J. APSADV.2021.100112.
- [32] E.I. Ross-medgaarden, I.E. Wachs, J. Phys. Chem. C 111 (2007) 15089–15099, https://doi.org/10.1021/jp074219c.
- [33] E. Wicke, Spectroscopy in Heterogeneous Catalysis, in: Von W. N. Delgass, G. L. Haller, R. Kellerman und J. H. Lunsford, Academic Press, New York 1979. X, 341 S., 117 Abb., geb., Angew. Chemie., 94 (1982) 324–325. (https://doi.org/10.100 2/ange.19820940446).
- [34] S. Xin, G. Liu, X. Ma, J. Gong, B. Ma, Q. Yan, Q. Chen, D. Ma, G. Zhang, M. Gao, Y. Xin, Appl. Catal. B Environ. 280 (2021), 119386, https://doi.org/10.1016/j. apcatb.2020.119386.
- [35] J. Feng, X. Hu, L.Y. Po, Environ. Sci. Technol. 38 (2004) 5773–5778, https://doi. org/10.1021/es049811j.
- [36] Q. Li, G. Wei, Y. Yang, Z. Li, L. Zhang, L. Shao, S. Lai, Catal. Sci. Technol. (2020), https://doi.org/10.1039/d0cy01539c.
- [37] A.N. Kofina, P.G. Koutsoukos, Cryst. Growth Design 5 (2005), https://doi.org/ 10.1021/cg049803e.
- [38] D.A. Svintsitskiy, T.Y. Kardash, O.A. Stonkus, E.M. Slavinskaya, A.I. Stadnichenko, S.V. Koscheev, A.P. Chupakhin, A.I. Boronin, J. Phys. Chem. C 117 (2013) 14588–14599, https://doi.org/10.1021/JP403339R.
- [39] H.S. Liu, K.J. Wang, X.Y. Cao, J.X. Su, Z. Gu, RSC Adv. 11 (2021) 12532–12542, https://doi.org/10.1039/d1ra00176k.
- [40] G.A. El-Shobaky, M. Mokhtar, A.M. Salem, Mater. Res. Bull. 40 (2005) 891–902, https://doi.org/10.1016/j.materresbull.2005.03.006.
- [41] T. Yi, C. Guo, S. Zhao, K. Zhan, W. Gao, L. Yang, G. Du, Eur. J. Wood Wood Prod. 783 (78) (2020) 471–482, https://doi.org/10.1007/S00107-020-01514-Z.
- [42] G. Cheng, A.R.Hight Walker, Anal. Bioanal. Chem 3963 (396) (2009) 1057–1069, https://doi.org/10.1007/S00216-009-3203-0.
- [43] D. Zhao, C.-M. Tu, X.-J. Hu, N. Zhang, RSC Adv. 7 (2017) 37596–37603, https://doi.org/10.1039/C7RA05950G.
- [44] J. Herney-Ramirez, M.A. Vicente, L.M. Madeira, Appl. Catal. B Environ. 98 (2010) 10–26, https://doi.org/10.1016/j.apcatb.2010.05.004.
- [45] S. Giannakis, Appl. Catal. B Environ. 248 (2019) 309–319, https://doi.org/
- [46] C. Angelici, F. Meirer, A.M.J. Van Der Eerden, H.L. Schaink, A. Goryachev, J. P. Hofmann, E.J.M. Hensen, B.M. Weckhuysen, P.C.A. Bruijnincx, ACS Catal. 5 (2015) 6005–6015. https://doi.org/10.1021/acscatal.5b00755.
- [47] C. Angelici, M.E.Z. Velthoen, B.M. Weckhuysen, P.C.A. Bruijnincx, ChemSusChem 7 (2014) 2505–2515, https://doi.org/10.1002/cssc.201402361.
- [48] A. Chakrabarti, I.E. Wachs, ACS Catal. 8 (2018) 949–959, https://doi.org/ 10.1021/acscatal.7b03598.
- [49] W.E. Taifan, T. Bučko, J. Baltrusaitis, J. Catal. 346 (2017) 78–91, https://doi.org/ 10.1016/j.jcat.2016.11.042.
- [50] F. Khairallah, A. Glisenti, M.M. Natile, A. Galenda, Surf. Sci. Spectra 19 (2012) 23–29, https://doi.org/10.1116/11.20071104.
- [51] P. Salvador, J.L.G. Fierro, J. Amador, C. Cascales, I. Rasines, J. Solid State Chem. 81 (1989) 240–249, https://doi.org/10.1016/0022-4596(89)90011-X.
- [52] A. Davó-Quiñonero, A. Davó-Quiñonero, A. Davó-Quiñonero, E. Bailón-García, S. López-Rodríguez, J. Juan-Juan, D. Lozano-Castelló, M. García-Melchor, F. C. Herrera, F.C. Herrera, E. Pellegrin, C. Escudero, A. Bueno-López, A. Bueno-López, ACS Catal. 10 (2020) 6532–6545, https://doi.org/10.1021/ acscatal 0c00648
- [53] S. Collado, L. Garrido, A. Laca, M. Diaz, Environ. Sci. Technol. 44 (2010) 8629–8635, https://doi.org/10.1021/es1021944.
- [54] D. Kiani, Y. Sheng, B. Lu, D. Barauskas, K. Honer, Z. Jiang, J. Baltrusaitis, ACS Sustain. Chem. Eng. 7 (2018) 1545–1556, https://doi.org/10.1021/ acssuschemeng.8b05318.
- [55] V.S. Birchal, S.D.F. Rocha, M.B. Mansur, V.S.T. Ciminelli, Can. J. Chem. Eng. 79 (2001) 507–511, https://doi.org/10.1002/cjce.5450790406.
- [56] M. Nie, Y. Li, J. He, C. Xie, Z. Wu, B. Sun, K. Zhang, L. Kong, J. Liu, New J. Chem. 44 (2020) 2847–2857, https://doi.org/10.1039/d0nj00125b.
- [57] M. Pirsaheb, S. Moradi, M. Shahlaei, N. Farhadian, New J. Chem. 44 (2020) 17735–17743, https://doi.org/10.1039/d0nj04014b.
- [58] N. Barhoumi, N. Oturan, S. Ammar, A. Gadri, M.A. Oturan, E. Brillas, Environ. Chem. Lett. 15 (2017) 689–693, https://doi.org/10.1007/s10311-017-0638-y.

- [59] Y. Wang, L. Rao, P. Wang, Z. Shi, L. Zhang, Appl. Catal. B Environ. 262 (2020), 118308, https://doi.org/10.1016/j.apcatb.2019.118308.
- [60] E. Yamal-Turbay, E. Jaén, M. Graells, M. Pérez-Moya, J. Photochem. Photobiol. A Chem. 267 (2013) 11–16, https://doi.org/10.1016/j.jphotochem.2013.05.008. [61] J. Jeong, W. Song, W.J. Cooper, J. Jung, J. Greaves, Chemosphere 78 (2010)
- 533-540, https://doi.org/10.1016/j.chemosphere.2009.11.024.
- [62] Y.Y. Chen, Y.L. Ma, J. Yang, L.Q. Wang, J.M. Lv, C.J. Ren, Chem. Eng. J. 307 (2017) 15-23, https://doi.org/10.1016/j.cej.2016.08.046.
- [63] G.B. Kauffman, J. Chem. Educ. 77 (2000) 165, https://doi.org/10.1021/
- [64] J.J. Bravo-Suárez, B. Subramaniam, R.V. Chaudhari, J. Phys. Chem. C 116 (2012)
- 18207–18221, https://doi.org/10.1021/jp303631v.
 [65] L. Nguyen, F.F. Tao, Y. Tang, J. Dou, X.J. Bao, Chem. Rev. 119 (2019) 6822–6905, https://doi.org/10.1021/acs.chemrev.8b00114.